THE JOURNAL OF PHYSICAL CHEMISTRY B
A JOURNAL OF THE AMERICAN CHEMICAL SOCIETY

pubs.acs.org/JPCB

Article

QM-Cluster Model Study of the Guaiacol Hydrogen Atom Transfer and Oxygen Rebound with Cytochrome P450 Enzyme GcoA

Qianyi Cheng* and Nathan J. DeYonker*

Cite This: *J. Phys. Chem. B* 2021, 125, 3296−3306

Read Online

ACCESS | Metrics & More | Article Recommendations | Supporting Information

ABSTRACT: The key step of the O-demethylation of guaiacol by GcoA of the cytochrome P450-reductase pair was studied with DFT using two 10-residue and three 15-residue QM-cluster models. For each model, two reaction pathways were examined, beginning with a different guaiacol orientation. Based on this study, His354, Phe349, Glu249, and Pro250 residues were found to be important for keeping the heme in a planar geometry throughout the reaction. Val241 and Gly245 residues were needed in the QM-cluster models to provide the hydrophobic pocket for an appropriate guaiacol pose in the reaction. The aromatic triad Phe75, Phe169, and Phe395 may be necessary to facilitate guaiacol migrating into the enzyme active site, but it does not qualitatively affect kinetics and thermodynamics of the proposed mechanism. All QM-cluster models created by *RINRUS* agree very well with previous experimental work. This study provides details for better understanding enzymatic O-demethylation of lignins to form catechol derivatives by GcoA.

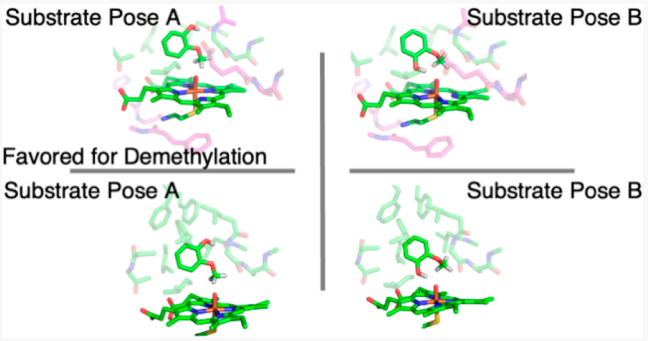

INTRODUCTION

Lignin, a class of complex organic polymers, is abundant in nature, especially in plants. It is rigid and does not degrade easily, so it is particularly important in the formation of wood and bark cell walls for structural and nutrient and water transport functions.[1] Chemically, lignin is hydrophobic, highly methylated, and rich in aromatic subunits. Three forms of lignin phenylpropanoids, *p*-hydroxyphenyl, guaiacyl, and syringyl, are composed of three main monolignol monomers, *p*-coumaryl alcohol, coniferyl alcohol, and sinapyl alcohol, respectively.[2] Though lignin is rich in carbon, it is not easy to break down into smaller fragments, and it is an under-utilized energy source. Efficiently catabolizing lignin, modifying the structures, and converting lignin into carbon and bioenergy sources has been an active research topic.[3,4]

Enzymatic lignin O-demethylation can remove the $-OCH_3$ group and lead to more accessible phenolic hydroxyl groups and further to various catechol derivatives. However, the reactions of various lignins by different enzymes have not been fully elucidated. The heterogeneity of lignins poses significant hurdles to biological processing to produce fine chemicals and/or biofuels.[5] Many enzymes that are known to demethylate lignin have limited capability to work with diverse lignin-derived substrates,[6−11] and substantial effort has been made to discover novel, less-selective enzymes.[6−10,12−16]

The superfamily of cytochrome P450 enzymes present in various organisms have been identified by their diverse chemical reactivity, such as C−H hydroxylation, sulfoxidation, and C═C epoxidation.[17−34] Activation of substrates by Compound 1 of cytochrome P450 (Cpd1, the Fe═O−porphyrin moiety) have short lifetimes that are difficult to characterize, thus many theoretical studies have supported experimental observation.[35−42] Cytochrome P450 has also been found to participate in lignin degradation.[43−45] Recently, a promising *Amycolatopsis* cytochrome P450-reductase pair (GcoAB, a two component P450 class composed of GcoA and GcoB) has been discovered,[46] which was shown by Beckham, McGeehan, Houk, DuBois, et al., to efficiently demethylate several lignin-derived monomers,[47] suggesting a broad substrate scope for lignin degradation and valorization. The k_{cat} of demethylation of guaiacol by GcoA was measured to be 6.8 ± 0.5 s^{-1} at 25 °C, identified as the rate limiting step in the coupled two-component catalytic process.

A reaction mechanism for guaiacol O-demethylation was proposed based on density functional theory (DFT) computations via optimization in the gas phase then single point energy calculations using an implicit solvent model,[47] in which two competitive pathways (paths A and B, outlined in Scheme 1 and 2) were explored using a QM-cluster model with only the Cpd1 (a porphyrin radical cation Fe^{IV}═O, as truncated heme),

Received: December 1, 2020
Revised: March 17, 2021
Published: March 30, 2021

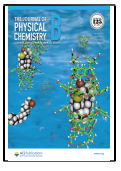

Scheme 1. Reaction Mechanism of 10-Residue Model and 15-Residue Model in Path A[a]

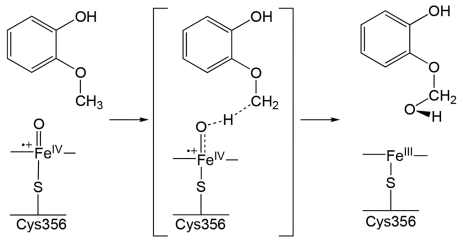

[a]Here the Cpd1-oxo ligand abstracts H from the guaiacol and led to a hemiacetal product.

Scheme 2. Reaction Mechanism of 10-Residue Model and 15-Residue Model in Path B[a]

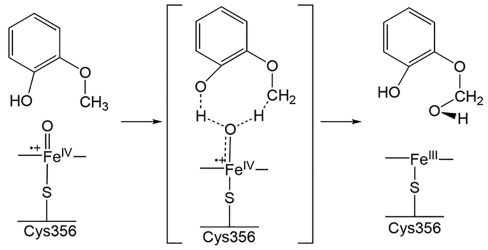

[a]Here the Cpd1-oxo ligand abstracts H from guaiacol and led to a hemiacetal product, different from ref 47, which led to the unproductive acetal product.

guaiacol, and part of the side chain of Cys356 (60 atoms total). The proposed mechanisms have different guaiacol orientations. The conformation of path A is similar to the enzyme−substrate form of the X-ray crystal structure, PDB ID: 5NCB. In path B, the hydroxyl group of guaiacol forms an intermolecular hydrogen bond with the oxo ligand of the heme. Both substrate poses were modeled by Beckham and collaborators via a 1 μs molecular dynamic (MD) simulation.[47]

In both pathways, doublet and quartet spin multiplicities of the model were considered (4 pathways in total).[47] The first step of hydrogen atom transfer (HAT) from the methoxy group of the substrate to Fe═O oxygen was found to be the rate-limiting step. Among the four transition states (TSs) along four pathways, TS1-b^2 (path B with the model in the doublet state) had the lowest free energy of activation, which is also closest to the experimentally predicted rate constant k_2 (6.8 ± 0.5 s^{-1} at 25 °C, ∼16.3 kcal mol^{-1}). The activation free energies of the TS1-a^2, TS1-a^4, TS1-b^2, TS1-b^4 were reported as 27.6, 18.9, 17.4, and 17.7 kcal mol^{-1}, respectively.[47] With similar rate-limiting activation free energies, TS1-a^4, TS1-b^2, and TS1-b^4 would be equally viable within the expected error of DFT computation. However, in their MD simulation, the guaiacol substrate mostly remained in the "path A" orientation,[47] suggesting that this pathway corresponds to the experimental mechanism. Also, the product of path B has a cyclic conformation which would not easily lead to the catechol, as there are no water molecules in the active site to form a hemiacetal that subsequently produces the experimentally observed catechol product. Despite clear evidence of the path A mechanism from both kinetic/crystallographic experiments and MD simulations, the QM-cluster model results in the original publication do not validate the experimentally proposed mechanism.

In a follow-up study of syringol degradation catalyzed by Cpd1 performed by Beckham and coauthors, similar QM-cluster models were employed.[16] The mechanism proposed in their work is that syringol similarly binds to Cpd1 productively via the substrate pose of path A. However, their QM-cluster model results again suggest that other substrate orientations can lead to undesired products via hydrogen atom transfer transition states with lower activation free energies than pathway A, again not consistent with experimental observation.

In another recent computational study of syringol degradation by GcoA by de Visser and coauthors,[48] QM-cluster models (302 atoms) were manually built based on one of the X-ray crystal structures reported by Beckham, McGeehan, Houk, DuBois et al. (PDB: 5OMU) with two ligand poses that also lead to two products via different proposed mechanisms. de Visser and coauthors found the two pathways to be competitive kinetically and thermodynamically, but only the pathway with the methoxy C−H of syringol pointing at Cpd1 leads to the hemiacetal product that can further produce a catechol. However, this path was predicted to be rate-limiting with a higher activation free energy (23.4 and 22.0 kcal mol^{-1} for the quartet and doublet spin states) than the earlier computations using guaiacol as substrate. The QM-cluster models of de Visser and coauthors thus indicate that demethylation of syringol would be slow, validating the kinetic experiments of Beckham, McGeehan, Houk, DuBois, et al. that show syringol can bind to the enzyme but does not show catalytic demethylation. Interestingly, de Visser and coauthors then created *in silico* mutants of the 5OMU X-ray crystal structure to suggest ways that the GcoA enzyme could be engineered to preferentially create demethylation products over acetal products.

In order to more appropriately validate experimental findings from the previous work and to formulate atomic-level enzyme models that allow exploration of structure−activity relationships of lignin valorization with GcoAB, larger QM-cluster models are necessary. Our group has employed Residue Interaction Networks (RINs)[49,50] to algorithmically generate QM-cluster models. RINs have been used in the context of QM-cluster modeling to study various enzymatic reactions.[51−54] The in-house software toolkit *Residue Interaction Network-based ResidUe Selector* (RINRUS) is under development to simplify and automate computational enzymology workflows. The size and shape of the QM regions are very important to consider when constructing models in computational enzymology[55,56] but general strategies have not been well characterized. Using the RINRUS toolkit to study fluctuation of structure and reactivity with respect to model size is an active area of research in our group but beyond the scope of this work. Here, we constructed QM-models of P450 GcoA by enumerating residue contacts and created five new QM-cluster models to better understand the O-demethylation reaction mechanism of guaiacol at the atomic-level.

COMPUTATIONAL METHODS

The X-ray crystal structure of the P450 GcoA (PDB ID: 5NCB) was used to construct the models for QM-cluster computations. In 5NCB, there is no oxygen atom above the Fe in the substrate HEM501. By aligning the Cpd1 (the Fe═O-porphyrin moiety) in the doublet spin state of the optimized DFT structure from ref 19 to the heme in 5NCB, an oxygen atom was added for model construction (O904, Figure 1a). Hydrogen atoms were added to backbone and side chain heavy atoms of the enzyme using the *reduce* program.[57] Hydrogen atoms were also manually added to

https://doi.org/10.1021/acs.jpcb.0c10761
J. Phys. Chem. B 2021, 125, 3296−3306

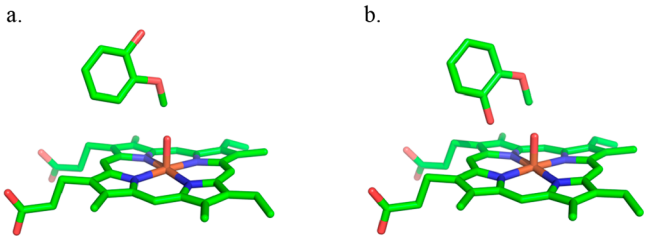

Figure 1. O-Demethylation of two guaiacol orientations was explored, in part a where the orientation of guaiacol is the same as in the X-ray crystal structure [PDB: 5NCB (path A)], and in part b, where the orientation of guaiacol allows hydrogen bonding between the substrate hydroxyl group and the heme oxo (path B). The oxygen atom (red sphere) is adopted from the doublet spin state of Cpd1 from the supporting material in ref 47.

the protoporphyrin IX (HEM501), and the cysteine residue (Cys356) which was bond to the iron and guaiacol (JZ3502). No protons were added to the carboxyl groups of HEM501 providing a neutral radical heme and cysteinate complex. The histidine residue (His354) close to one of the carboxylate groups was doubly protonated. Next, the protonated PDB file was processed by *probe*[58] to generate the RIN based on noncovalent interatomic contact interaction by rolling a spherical probe (using the default radius = 0.25 Å) over the van der Waals surface of the molecule to detect different types of interactions. Additionally, pose B of the substrate JZ3502 was generated by replacing the hydroxyl group and hydrogen atom on the ring next to the methoxy group so that O904 is positioned between the methoxy and hydroxyl group of JZ3502 (Figure 1b). Like in the computations by Beckham, McGeehan, Houk, DuBois, et al.,[47] two potential spin multiplicities of the models (doublet and quartet) were considered. A list of residues used and frozen atoms in each QM-cluster model is provided in Table 1.

The first set of QM-cluster models was constructed with a "seed" composed of the active site substrates HEM501, JZ3502, and O904. In total, 36 residues (including two crystallographic waters that interact with HEM501 and are not close to O904) were identified from chain A that directly interact with HEM501, JZ3502, or O904 via either hydrogen bonds, atomic overlaps (steric clashes), or van der Waals contacts (close contacts).[58] Based on the residues generated by a given RIN set, either main chain, side chain, or entire residues were trimmed and treated to fulfill atom valency in the model. Including the three seed fragments (HEM501, JZ3502 and O904), the largest possible "maximal" model contains 601 atoms, which is an intractable size. In order to make the computations more feasible, smaller sized models were built by including a set number of residues with diminishing count of contacts with the seed. According to the total counts of the atomic contacts, two models were selected for this study: one model with 10 residues (221 atoms; 12 C_α and 2 C_β atoms were kept frozen) and the other with 15 residues (282 atoms; 17 C_α and 2 C_β atoms were kept frozen), named model **1−10** and model **1−15** in short and were used to explore the reaction mechanism of guaiacol O-demethylation in GcoA. The 2D structure of the **1−10** and **1−15** QM-cluster models are shown in Figure 2, where the trimming scheme is demonstrated in Table S1. In the **1−10** model, the important residue Cys356 (where the sulfur is bond to Fe and considered as a "pin" holding the HEM501) as mentioned in ref 47 was included; while in the **1−15** model, another important residue Gly245 (where the amide nitrogen group is believed to coordinate with the oxygen atom of JZ3502) was also included.

A third QM-cluster model was constructed by using only substrate JZ3502 as the seed (Table 1), and a total of 15 residues were identified in this RIN. The entire set of 15 residues was used to construct the **2−15** model (271 atoms), with 14 C_α and 5 C_β atoms kept frozen. A fourth model was constructed that

Table 1. Residue and Trimming Information for the Various QM-Cluster Models of P450 GcoA Built in This Study[a]

model	**1−10** model	**1−15** model	**2−10** model	**2−15** model	**3−15** model
PHE75				C_α C_β	C_α C_β
ILE81		C_α	C_α	C_α	C_α
PHE169				C_α C_β	C_α C_β
VAL241	C_α	C_α	C_α	C_α	C_α
LEU244				C_α	C_α
GLY245		C_α	C_α	C_α	C_α
ALA246	C_α	C_α	C_α	C_α	C_α
GLU249		C_α			
PRO250		C_α			
ILE292	C_α C_β	C_α C_β	C_α C_β	C_α C_β	C_α C_β
ALA295				C_α	C_α
THR296	C_α C_β	C_α C_β	C_α C_β	C_α C_β	C_α C_β
PHE349	C_α	C_α			
HIS354	C_α	C_α			
ALA355					
CYS356	C_α	C_α	C_α	C_α	C_α C_β
PHE395				C_α C_β	C_α C_β
WAT689		X			
HEM501	X	X	X	X	X
JZ3502	X	X	X	X	X
O904	X	X	X	X	X

[a]"C_α" indicates frozen α-carbon atoms for that residue, "C_α C_β" indicates frozen α- and β-carbons for that residue, and "X" indicates that the specified non amino acid residue fragment is included in the model.

https://doi.org/10.1021/acs.jpcb.0c10761
J. Phys. Chem. B 2021, 125, 3296−3306

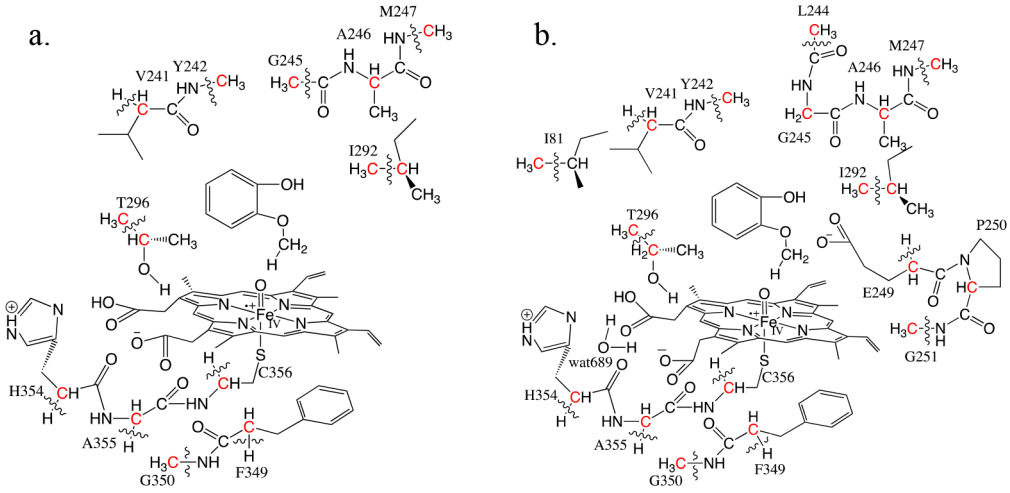

Figure 2. 2D structure of the **1−10** (a) and **1−15** (b) QM-cluster models based on PDB: 5NCB. One proton on His354 is shifted to the heme. The 14 and 19 frozen carbon atoms in the **1−10** and **1−15** models are colored in red, respectively. The wavy lines indicate truncation of the residue at C_α.

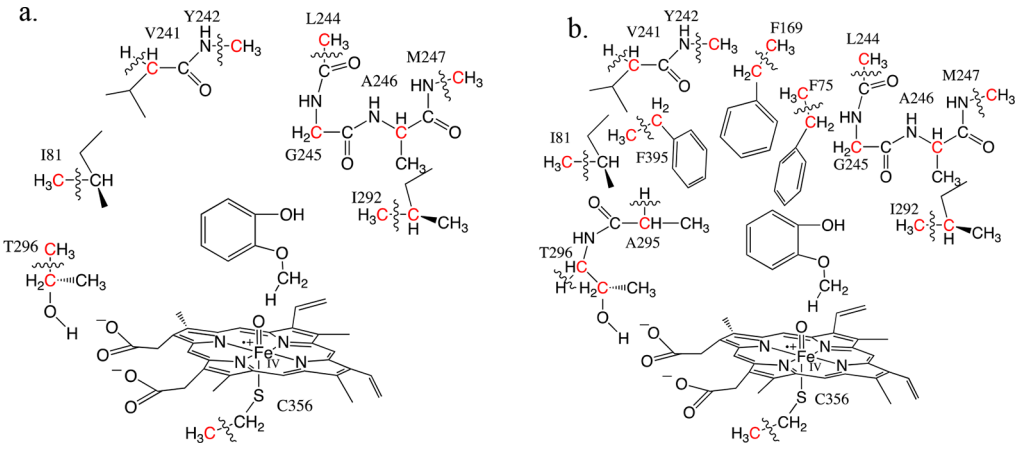

Figure 3. 2D structure of the **2−10** (a) and **2−15** (b) QM-cluster models based on PDB: 5NCB. The 12 and 19 frozen carbon atoms in the **2−10** and **2−15** models are colored in red, respectively. The **3−15** model is equivalent to the **2−15** model but with one extra C_β on Cys365 kept frozen. The wavy lines indicate truncation of the residue at C_α.

includes all residues common to both **1−15** and **2−15** models. Fortuitously, there are ten residues (Ile81, Val241, Gly245, Ala246, Ile292, Thr296, Cys356, HEM501, JZ3502, and O904) in this model, **2−10** with 195 atoms and 10 C_α and 2 C_β atoms kept frozen. A fifth 15-residue model (**3−15**) was also constructed with the exact same residues and number of atoms as the **2−15** model but with the Cys356 C_β atom frozen. The 2D structure of the **2−10** and **2−15** QM-cluster models are shown in Figure 3, where the trimming scheme is also demonstrated in Table S2.

All quantum mechanical cluster model computations were performed using the using the Gaussian16 program.[59] Density functional theory (DFT) with the hybrid B3LYP exchange-correlation functional[60,61] was employed with the 6-31G(d′) basis set for N, O, and S atoms,[62−64] with the modified Hay and Wadt basis set and LANL2DZ effective core potential (ECP)[65−67] on Fe and the 6-31G basis sets for C and H atoms.[68] QM-cluster models incorporated the Grimme D3 (Becke−Johnson) dispersion correction (GD3BJ)[69,70] and implicit solvation via the conductor-like polarizable continuum model (CPCM)[71,72] using universal force field (UFF) atomic radii, a nondefault electrostatic scaling factor of 1.2, and the default parameters for water with an attenuated dielectric constant of $\varepsilon = 4$. This dielectric constant value has been previously determined as appropriate for simulating the less-polarized environment within an enzyme active site.[73,74] Unscaled harmonic vibrational frequency calculations were used to identify all stationary points as either minima (no imaginary frequencies) or transition states (TSs, only one imaginary frequency). TSs were located first for each elementary step of the proposed mechanism; the reactants and products were then located by following the intrinsic reaction coordinate (IRC).[75,76] It is important to note that our group uses the "freeze code" scheme in Gaussian16, where all Hessian elements are zero when involving two frozen Cartesian coordinates. The phenomenon where several small magnitude imaginary vibrational frequencies appear in the thermochemical analysis does not arise in our treatment of the Hessian matrix. Zero-point energies (ZPE) and thermal enthalpy/free energy corrections were computed at 1 atm and 298.15 K.

RESULTS AND DISCUSSION

Mechanistic labels in our study obey the following scheme: **WX−Y-Z**^{n}; where **W** = R (reactant), TS (transition state), or P (product); ***X*** = model number (1, 2, or 3); ***Y*** = no. of residues in

https://doi.org/10.1021/acs.jpcb.0c10761
J. Phys. Chem. B 2021, 125, 3296−3306

the model (10 or 15); **Z** = path A or B; ***n*** = spin multiplicity of the QM-cluster model. The previously reported computations suggested a two-step HAT mechanism, where a radical cation guaiacol intermediate exists before facile conversion to hemiacetal product. This zwitterionic intermediate is possible via gas phase geometry optimizations of the QM-cluster model (corresponding to the computational method used by Beckham, McGeehan, Houk, DuBois, et al.) but is not observed in our computations where implicit solvation is accounted for throughout.

The 1−10 and 1−15 Models. 3D overlays of optimized reactants in the doublet (in green) and quartet (in magenta) spin state from each model are aligned to the template from the X-ray crystal structure (in yellow, where the initial position of O904 is adopted from ref 47) and shown in Figures S1 and S2. Important bond distances for the reactant, TS, and product in all models via path A and B can be found in Tables S3 and S4.

The computed Fe−O bond distances (1.63−1.64 Å) and Fe−S bond distances (2.49−2.54 Å) of the reactants in all QM-cluster models show a double bond character as in the thiolate-ligated oxoiron(IV) in cytochrome P450 Fe^{IV}═O.[77−79] Protonation of a carboxylate group of HEM501 is energetically favored compared to double protonation of His354, and this protonation state is observed in all optimized reactants, TSs, and products in the **1−10** and **1−15** models. The other carboxylate group of HEM501 is stabilized by the hydroxyl group of the Thr296 side chain, and the Cpd1 stayed flat as seen in the heme radical cation complex. In the X-ray crystal structure, Fe is located in the center of the heme with square pyramidal coordination, bonding to the four nitrogen atoms of the heme and the S atom of Cys356. The heme is puckered in the X-ray crystal structure, while in our computed **1−10** and **1−15** reactant models the Fe(IV) ion is octahedrally coordinated to the more planar heme, the Cys356 S atom, as well as the oxo ligand (O904). The Phe349 residue "below" the heme translates up toward heme to form a better aromatic interaction with the aromatic rich substrate. The interactions between the two oxygen atoms of guaiacol and Val241 backbone carbonyl as well as Gly245 amide nitrogen atom keep the substrate well positioned in the active site. Along the reaction paths in each of the models, large geometric changes in the TS and product are seen in the substrates (Tables S3 and S4).

The reaction mechanism via path A and B are shown in Scheme 1 and 2, as well as Figures 4 and 5 which are illustrated

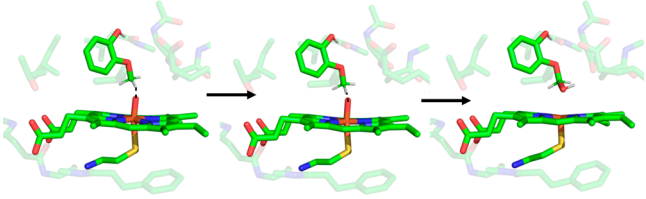

Figure 4. Guaiacol O-demethylation via path A. The figure shows the path using the **1−15-A^4** model. The **1−10-A^4**, **1−10-A^2**, and **1−15-A^2** models follow the same mechanism.

using the **1−15-A^4** and **1−15-B^4** model. In path A, a hydrogen atom on the methoxy C−H group of guaiacol is transferred to the oxo ligand, followed by the radical rebound[17,29,80] of the oxygen in Fe═O−H to the newly formed CH_2 radical carbon of guaiacol, forming a low energy hemiacetal product. This is seen in the transition state and IRCs of both the quartet and doublet

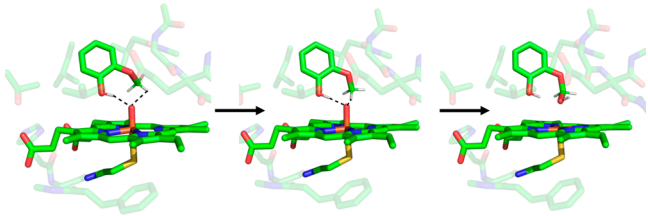

Figure 5. Guaiacol O-demethylation via path B. The figure shows the path using the **1−15-B^4** model. The **1−10-B^4**, **1−10-B^2**, and **1−15-B^2** models follow the same mechanism.

spin state models. The hydrogen atom transfer mechanism is also observed via path B. Even though the hydrogens from the OH and CH_3 group in guaiacol form two hydrogen bonds with O904, the cyclic TSs of path B also lead to a low energy hemiacetal product.

The free energy diagrams of **1−10-A$^{2/4}$**, **1−10-B$^{2/4}$**,**1−15-A$^{2/4}$**, and **1−15-B$^{2/4}$** are shown in Figure 6 and tabulated in Table S5. In the **1−10** models, **R1−10-A^2** has the lowest free energy, so it is set as the reference energy point (ΔG = 0.0 kcal mol^{-1}). The energy difference between **R1−10-A^2** and **R1−10-A^4** is less than 1.0 kcal mol^{-1}. However, the path B (doublet and quartet) reactant structures are thermodynamically unfavorable compared to their path A counterparts by 5.2−13.2 kcal mol^{-1} in model **1−10** and 6.5−15.6 kcal mol^{-1} in model **1−15**. In the study by Beckham, McGeehan, Houk, DuBois, et al., the reactant of the doublet spin state was only 0.2 kcal mol^{-1} lower in energy in their path A than the quartet spin state.[47] The large energy difference between the reactants in paths A and B in our study better agrees with the observation in the earlier MD simulations and the X-ray crystal structure of a "path A-like" guaiacol orientation. The free energies of activation of the four pathways are 10.6, 10.3, 20.0, and 20.0 kcal mol^{-1} for **1−10-A^2**, **1−10-A^4**, **1−10-B^2**, and **1−10-B^4**, respectively. The free energies of reaction are greatly exergonic, equal to −52.9, −53.6, −45.1, and −49.7 kcal mol^{-1} for the four models/spin multiplicities, respectively. Considering both reactant energies and free energies of activation, path A is clearly more thermodynamically and kinetically favorable than path B, for models with the Cpd1 in either doublet or quartet spin multiplicities.

For the **1−15** model, reactants in path A are still lower in free energy than in path B, again with nearly isoenergetic **R1−15-A^2** and **R1−15-A^4** structures. Here, **R1−15-A^4** is defined as the free energy baseline (ΔG = 0.0 kcal mol^{-1}). For path B, reactants are again higher in free energy than path A reactants. Interestingly, the addition of 5 extra residues destabilizes the effective activation free energies ($\Delta G^{\ddagger}$ = 15.9 kcal mol^{-1} for **TS1−15-A^4** and 15.7 kcal mol^{-1} for **TS1−15-A^2**), bringing the predicted values in agreement with the experimentally observed kinetics and earlier QM/MM studies with various functionals and basis sets (19.5−21.8 kcal mol^{-1}).[81,82] The computed reaction free energies (Figure 6) are again largely exergonic and two lower energy products **P1−15-A^4** and **P1−15-A^2** lead to reaction free energies of −56.1 and −55.7 kcal mol^{-1}, which also suggests path A products are more thermodynamically favorable. The inclusion of Gly245 in the **1−15** model (along with Val241, which is in both **1−10** and **1−15** models) provides important hydrophobic interactions between residue side chains and the aromatic ring of the guaiacol substrate.[47]

The 2−10 and 2−15 Models. The **2−10** and **2−15** P450 GcoA models differ from the **1−10** and **1−15** models by ranking

https://doi.org/10.1021/acs.jpcb.0c10761
J. Phys. Chem. B 2021, 125, 3296−3306

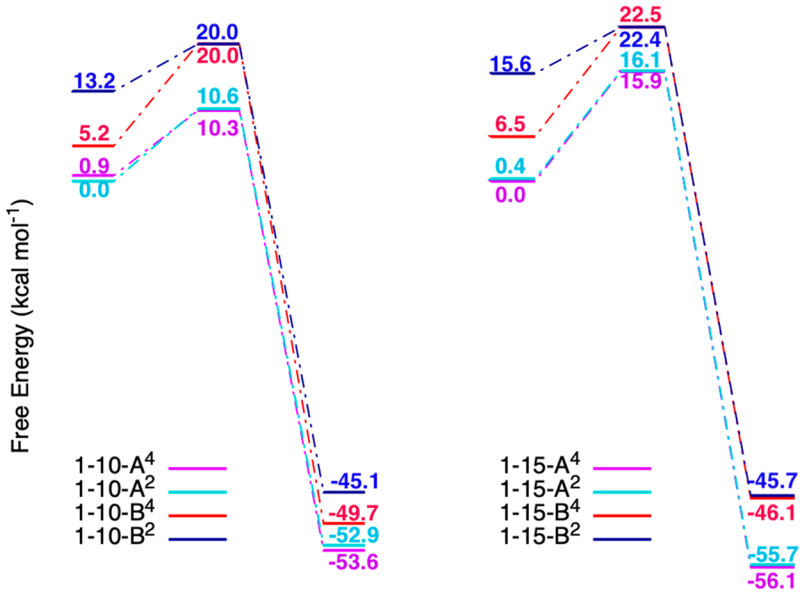

Figure 6. Free energy diagram of **1−10** models and **1−15** models. (a, left) Path via **1−10-A^4** in magenta, **1−10-A^2** in turquoise, **1−10-B^4** in red, and **1−10-B^2** in dark blue; (b, right) Path via **1−15-A^4** in magenta, **1−15-A^2** in turquoise, **1−15-B^4** in red, and **1−15-B^2** in dark blue. Gibbs free energies are given in kcal mol^{-1}.

residues in RINRUS that only interact with the guaiacol substrate rather than residues that interact with either guaiacol or the heme. 3D overlays of optimized reactants in the doublet (in green) and quartet (in magenta) spin state from each model are aligned to the template from the X-ray crystal structure (in yellow and shown in Figures S3 and S4). Similar to the **1−10** and **1−15** models, the computed Fe−O bond distances (1.63 Å) and Fe−S bond distance (2.49−2.56 Å) of the reactants are found in all **2−10** and **2−15** models. The demethylation occurs via hydrogen atom transfer from the H of guaiacol methoxy C−H group to the O904, and then the hydroxyl group comes off from the Fe ion and bonds to the CH_2 radical on guaiacol (Figures 7 and 8). The heme in the geometry optimized

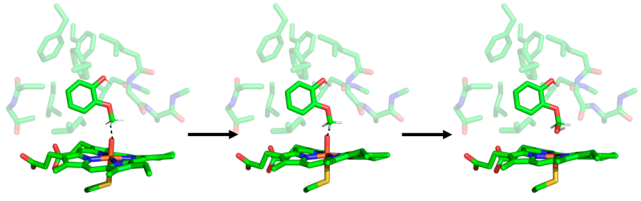

Figure 7. Guaiacol O-demethylation via path A. The figure shows the path using the **2−15-A^4** model. The **2−10-A^4**, **2−10-A^2**, and **2−15-A^2** models follow the same mechanism.

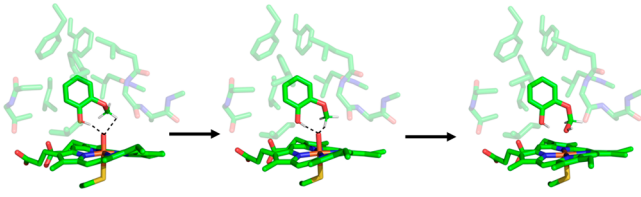

Figure 8. Guaiacol O-demethylation via path B. The figure shows the path using the **2−15-B^4** model. The **2−10-B^4**, **2−10-B^2**, and **2−15-B^2** models follow the same mechanism.

reactants, TSs, and product are puckered and slightly tilted. In these models, there are no residues such as His354, Phe349, Glu249, and Pro250 "under" the heme to fully stabilize carboxylic groups on the periphery of the heme. As the heme is part of the seed in some of our models, we decided early on to not artificially trim the carboxylic functional groups, as was done by Beckham, McGeehan, Houk, DuBois, et al.; and the Cpd1-cystinate complex is a neutral radical.

The free energy diagrams of **2−10-A$^{2/4}$**, **2−10-B$^{2/4}$**, **2−15-A$^{2/4}$**, and **2−15-B$^{2/4}$** are shown in Figure 9 and tabulated in Table S6. Interestingly, the **2−10** model has the same 10 residues "above" the heme as those in the **1−15** model. The overall kinetics and thermodynamics of these two models are similar for paths A and B. The doublet and quartet spin **2−10-A** reactants, transition states, and products are isoenergetic to within 1.2 kcal mol^{-1}, and the demethylation reaction is extremely exergonic. Both spin multiplicities of the **2−10-B** pathway have reactants higher in free energy than **2−10-A** reactants, and transition state energies are 5.5 to 6.7 kcal mol^{-1} higher in free energy than their path A counterparts.

The **2−15** model should be more reliable than models previously discussed because it contains the triad of phenylalanine residues (Phe75, Phe169, Phe395), which were hypothesized in ref 47 to play a crucial role in substrate positioning. The free energy diagram (Figure 9, right) is similar to that in the **1−10**, **1−15**, and **2−10** models. **R2−15-A^4** has the lowest free energy among the four reactants. The **R2−15-A^2** structure is nearly energetically degenerate at less than 0.5 kcal mol^{-1} higher in energy, but the path B reactants are much higher in free energy. Small free energy differences can be found in the TSs and products in path A. The low barrier of **2−15-A^4** (12.6 kcal mol^{-1}) is closer to the quartet spin state hydroxylation reaction predicted by Friesner et al. in a QM/MM study (11.7 kcal mol^{-1});[83] while in path B both doublet and quartet spin states have much higher activation free energies but lower reaction energies. Therefore, path A is favored by both computed kinetics and thermodynamics. The activation free energy differences between the **1−10/1−15** and **2−10/2−15** could be the result of a cation radical versus neutral radical character of the Cpd1-cystinate complex.

https://doi.org/10.1021/acs.jpcb.0c10761
J. Phys. Chem. B 2021, 125, 3296−3306

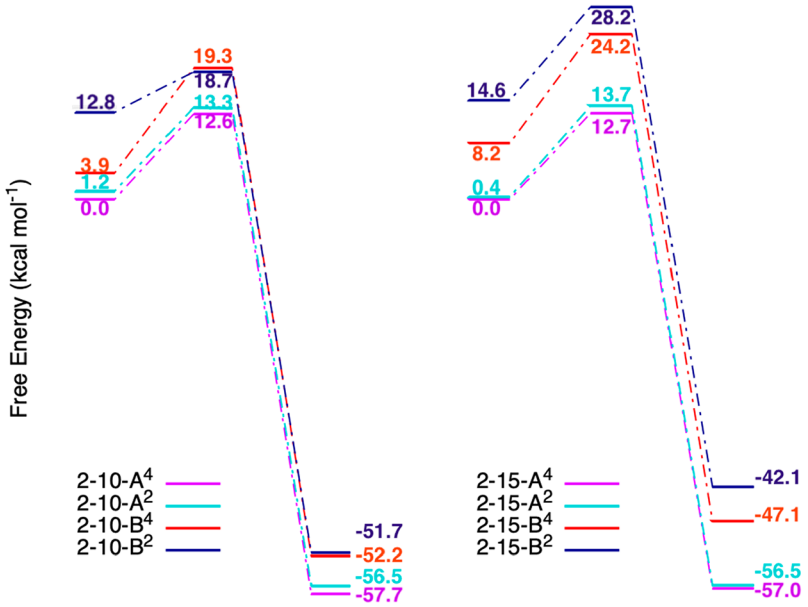

Figure 9. Free energy diagram of **2−10** models and **2−15** models. (a, left) Path via **2−10-A^4** in magenta, **2−10-A^2** in turquoise, **2−10-B^4** in red, and **2−10-B^2** in dark blue. (b, right) Path via **2−15-A^4** in magenta, **2−15-A^2** in turquoise, **2−15-B^4** in red, and **2−15-B^2** in dark blue. Gibbs free energies are given in kcal mol^{-1}.

The 3−15 Model. Among the residues that interact "below" the heme, only the side chain of Cys356 is kept in the **2−15** model. There was concern about the relatively large geometric changes seen in both heme and guaiacol in the **2−15** model compared to the **1−15** model. We proposed that the heme moiety may become less distorted if there were more constraints on the Cys356 residue. A third 15-residue model (**3−15**) was built equivalent to the **2−15** model but with both the C_α and C_β atoms of Cys356 frozen in their crystallographic positions. 3D overlays of optimized reactants in the doublet (in green) and quartet (in magenta) spin state from each model are aligned to the template from the X-ray crystal structure (in yellow) and are shown in Figure S5.

Though in the **3−15** model the heme is still slightly puckered and tilted, it is slightly less so than in the geometry optimized structures of model **2−15** (the aligned optimized reactants of **2−15** and **3−15** structures are shown in Figure S6). Overall, the guaiacol substrate is more constrained, but critical bond lengths in the reactants, TSs, and products are similar to those in the **2−15** models (Figures 10 and 11).

The additional atomic constraint on Cys356 generates a similar reaction free energy profile. The free energy diagram of **3−15-A/B** is shown in Figure 12 and tabulated in Table S7. **R3−15-A^4** has been found to be the lowest energy reactant but is only 0.7 kcal mol^{-1} lower in energy than **R3−15-A^2**. Similar to

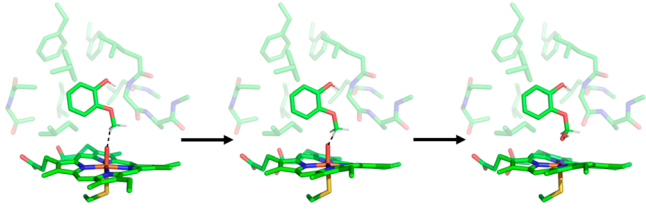

Figure 10. Guaiacol O-demethylation via path A. The figure shows the path using the **3−15-A^4** model. The **3−15-A^2** model follows the same mechanism.

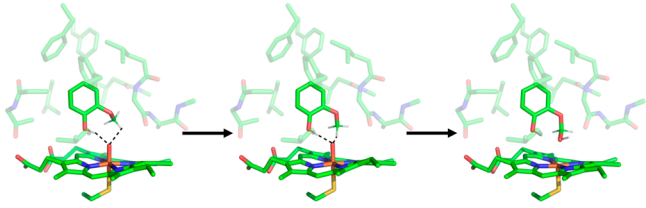

Figure 11. Guaiacol O-demethylation via path B. The figure shows the path using the **3−15-B^4** model. The **3−15-B^2** model follows the same mechanism.

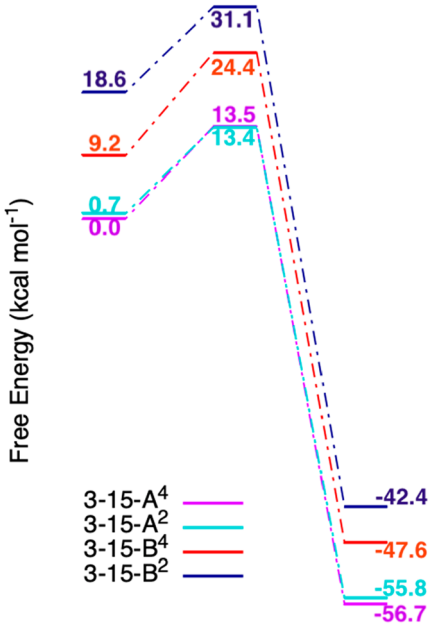

Figure 12. Free energy diagram of **3−15** models. Path via **3−15-A^4** in magenta, **3−15-A^2** in turquoise, **3−15-B^4** in red, and **3−15-B^2** in dark blue. Gibbs free energies are given in kcal mol^{-1}.

https://doi.org/10.1021/acs.jpcb.0c10761
J. Phys. Chem. B 2021, 125, 3296−3306

the model **2−15** free energy diagram, both path B reactants are thermodynamically disfavored by more than 9 kcal mol^{-1}. Unlike model **2−15**, the **TS3−15-A**^{4} is 0.1 kcal mol^{-1} higher in free energy than **TS3−15-A**^{2}. Calculated kinetics and thermodynamics of the QM-cluster models indicate that path A is more favored. All of the evidence supports the experimental observation that guaiacol can be effectively demethylated by GcoA. These results clearly agree with experimental observations and MD simulations of Beckham, McGeehan, Houk, DuBois, et al., unlike the small QM-cluster models used by their team.

CONCLUSIONS

Two 10-residue models and three 15-residue models are built to study the O-demethylation of guaiacol with cytochrome P450 GcoA. For each model, two reaction pathways are examined beginning with a different guaiacol orientation. The reactants in path A are always lower in energy than those in path B in all models explored in this study. The conformation of guaiacol in path A matches the MD simulation conducted by Beckham, McGeehan, Houk, DuBois, et al. where the methoxy C−H is pointing toward Cpd1 and the hydroxyl group is pointing away from Cpd1. All models lead to the preferred hemiacetal product which further leads to the final catechol product. Considering all QM-cluster models of path A, the differences in free energy of activation between the doublet and quartet spin state models are often less than 1.0 kcal mol^{-1}, and the relative free energies of doublet/quartet reactant structures are always less than 2.0 kcal mol^{-1}. Thus, facile spin crossover at all stages of the demethylation reaction is possible.

Overall, including as many residues that interact with the QM-cluster model "seed" as possible will improve the reliability of proposed mechanisms. In this study, the GcoA P450 active site is quite large, especially when including the heme as part of the seed. The full RINRUS-derived 39-residue QM-cluster model would account for the appropriate guaiacol binding pocket and better enforce planarity of the heme, but at 601 atoms is computationally intractable. Smaller models containing 10 amino acid residues around the seed are not quite satisfactory. For example, the **1−10** model appears to give an underestimation of the path A free energy of activation. By adding Gly245, Glu249, Pro250, and WAT689 to the model to generate model **1−15**, the computed free energies of activation are in very good agreement with the experimentally determined activation free energy of ∼16.3 kcal mol^{-1}, and the unproductive path B is not kinetically favored. Gly245, which is included in all models except **1−10**, was singled out as an important residue for posing guaiacol in the hydrophobic pocket. The doubly protonated His354 near one of the carboxylate groups may also be also important for sustaining Fe^{IV}═O heme radical cation character for the reaction.

The **2−10**, **2−15**, and **3−15** models have path A activation free energies (12.6−13.7 kcal mol^{-1}) that are slightly lower than experiment but are in good agreement considering factors involved in accurately simulating experimental rate constants with Density Functional Theory. Residues directly interacting with the heme may be important for electronically and sterically "pinning" the ligand in the active site and maintaining the proper coordination chemistry of the Fe ion. Our final model (**3−15**), is a variation of **2−15** with one extra frozen atom (C_β of Cys356). The heme is slightly less puckered in model **3−15**, but the guaiacol-heme interactions appear to be better described. From models **2−15** and **3−15**, the mechanism of path B is shown to be kinetically and thermodynamically implausible. This is a substantially different result than that predicted by the minimally sized QM-cluster model used in previous work, which did not contain any of the crucial hydrogen bonding between the active site residues and the guaiacol that would stabilize the path A transition state and destabilize the path B transition state. Previous computations of GcoA also show additional intermediates along the proposed mechanism. These intermediates exhibit unrealistic charge separation arising from gas phase geometry optimization of QM-cluster models then computing implicitly solvated single point energies at the gas phase stationary points. These minima and connecting transition states are not observed when the QM-cluster model workflow incorporates implicit solvation into geometry optimizations and harmonic vibrational frequency calculations. Considering all the models explored in our study and comparing to the models in ref 47, the small QM-cluster model employed by Beckham, McGeehan, Houk, et al. does not fully preserve the electronic structure of the reaction active site environment, as many important residues are not present in their model.

Our study provides a strong case that computational design to improve biodegradation processes can only proceed when based on reliable enzyme models with a well-constructed QM region. The RINRUS software toolkit provides automated construction of QM-cluster models with a reproducible workflow. RINRUS code is open-source but currently only available to readers by request until protocols and case studies are introduced in forthcoming publications. Once publicly released, RINRUS may be greatly beneficial to the computational enzymology community. For example, RINRUS-derived models could be used to validate and accelerate bioengineering of GcoA P450 to increase its catalytic prowess, or to perform high-throughput computational assays of possible lignin substrates. Our laboratories are still planning improvements to RINRUS, as our investigation of GcoA P450 proves that QM-cluster modelers must still take great care to identify "seed" residues in the protein active site.

ASSOCIATED CONTENT

Supporting Information

The Supporting Information is available free of charge at https://pubs.acs.org/doi/10.1021/acs.jpcb.0c10761.

Tables S1 and S2, lists of residues included in the optimized QM cluster models; Tables S3 and S4, bond distances of optimized reactants, transition states, and products in paths A and B; Tables S5−S7, reaction free energies; Table S8, absolute (free) energies; and Figures S1−S6, aligned optimized reactants (PDF)

Cartesian coordinates of the optimized stationary points along the reaction pathways, where all *xyz*-formatted files are contained in the archive and the charge of the **1−10** model is +1 and charges of all other models are 0 (ZIP)

AUTHOR INFORMATION

Corresponding Authors

Qianyi Cheng − *Department of Chemistry, University of Memphis, Memphis, Tennessee 38152, United States;* orcid.org/0000-0002-4640-2238; Email: qcheng1@memphis.edu

Nathan J. DeYonker − *Department of Chemistry, University of Memphis, Memphis, Tennessee 38152, United States;*

https://doi.org/10.1021/acs.jpcb.0c10761
J. Phys. Chem. B 2021, 125, 3296−3306

orcid.org/0000-0003-0435-2006; Email: ndyonker@memphis.edu

Complete contact information is available at: https://pubs.acs.org/10.1021/acs.jpcb.0c10761

Notes

The authors declare no competing financial interest.

■ ACKNOWLEDGMENTS

This work was supported by start-up funding from the University of Memphis Department of Chemistry and the National Science Foundation (CAREER) BIO-1846408. The High Performance Computing Center and the Computational Research on Materials Institute at The University of Memphis (CROMIUM) also provided generous resources for this research. The authors also thank Gregg Beckham, Heather Mayes, and Brandon Knott (NREL) and Marc Garcia-Borràs (UCLA) for assistance.

■ REFERENCES

(1) Sarkanen, K.; Ludwig, C. In *Lignins: Occurrence, Formation, Structure and Reactions - University of Kentucky*; Sarkanen, K. V., Ludwig, C. H., Eds.; Wiley-Interscience: New York, 1971.

(2) Boerjan, W.; Ralph, J.; Baucher, M. Lignin Biosynthesis. *Annu. Rev. Plant Biol.* **2003**, *54* (1), 519−546.

(3) Venkatesagowda, B. Enzymatic Demethylation of Lignin for Potential Biobased Polymer Applications. *Fungal Biol. Rev.* **2019**, *33* (3−4), 190−224.

(4) Fetherolf, M. M.; Levy-Booth, D. J.; Navas, L. E.; Liu, J.; Grigg, J. C.; Wilson, A.; Katahira, R.; Beckham, G. T.; Mohn, W. W.; Eltis, L. D. Characterization of Alkylguaiacol-Degrading Cytochromes P450 for the Biocatalytic Valorization of Lignin. *Proc. Natl. Acad. Sci. U. S. A.* **2020**, *117* (41), 25771−25778.

(5) Beckham, G. T.; Johnson, C. W.; Karp, E. M.; Salvachúa, D.; Vardon, D. R. Opportunities and Challenges in Biological Lignin Valorization. *Curr. Opin. Biotechnol.* **2016**, *42*, 40−53.

(6) Segura, A.; Bünz, P. V.; D'Argenio, D. A.; Ornston, L. N. Genetic Analysis of a Chromosomal Region Containing VanA and VanB, Genes Required for Conversion of Either Ferulate or Vanillate to Protocatechuate in Acinetobacter. *J. Bacteriol.* **1999**, *181* (11), 3494−3504.

(7) Morawski, B.; Segura, A.; Ornston, L. N. Substrate Range and Genetic Analysis of Acinetobacter Vanillate Demethylase. *J. Bacteriol.* **2000**, *182* (5), 1383−1389.

(8) Masai, E.; Sasaki, M.; Minakawa, Y.; Abe, T.; Sonoki, T.; Miyauchi, K.; Katayama, Y.; Fukuda, M. A Novel Tetrahydrofolate-Dependent O-Demethylase Gene Is Essential for Growth of Sphingomonas Paucimobilis SYK-6 with Syringate. *J. Bacteriol.* **2004**, *186* (9), 2757−2765.

(9) Abe, T.; Masai, E.; Miyauchi, K.; Katayama, Y.; Fukuda, M. A Tetrahydrofolate-Dependent O-Demethylase, LigM, Is Crucial for Catabolism of Vanillate and Syringate in Sphingomonas Paucimobilis SYK-6. *J. Bacteriol.* **2005**, *187* (6), 2030−2037.

(10) Yoshikata, T.; Suzuki, K.; Kamimura, N.; Namiki, M.; Hishiyama, S.; Araki, T.; Kasai, D.; Otsuka, Y.; Nakamura, M.; Fukuda, M.; Katayama, Y.; Masai, E. Three-Component O -Demethylase System Essential for Catabolism of a Lignin-Derived Biphenyl Compound in Sphingobium Sp. Strain SYK-6. *Appl. Environ. Microbiol.* **2014**, *80* (23), 7142−7153.

(11) Masai, E.; Katayama, Y.; Fukuda, M. Genetic and Biochemical Investigations on Bacterial Catabolic Pathways for Lignin-Derived Aromatic Compounds. *Biosci., Biotechnol., Biochem.* **2007**, *71* (1), 1−15.

(12) Karlson, U.; Dwyer, D. F.; Hooper, S. W.; Moore, E. R. B.; Timmis, K. N.; Eltis, L. D. Two Independently Regulated Cytochromes P-450 in a Rhodococcus Rhodochrous Strain That Degrades 2-Ethoxyphenol and 4-Methoxybenzoate. *J. Bacteriol.* **1993**, *175* (5), 1467−1474.

(13) Eltis, L. D.; Karlson, U.; Timmis, K. N. Purification and Characterization of Cytochrome P450RR1 from Rhodococcus Rhodochrous. *Eur. J. Biochem.* **1993**, *213* (1), 211−216.

(14) Harada, A.; Kamimura, N.; Takeuchi, K.; Yu, H. Y.; Masai, E.; Senda, T. The Crystal Structure of a New O-Demethylase from Sphingobium Sp. Strain SYK-6. *FEBS J.* **2017**, *284* (12), 1855−1867.

(15) Kohler, A. C.; Mills, M. J. L. L.; Adams, P. D.; Simmons, B. A.; Sale, K. L. Structure of Aryl O -Demethylase Offers Molecular Insight into a Catalytic Tyrosine-Dependent Mechanism. *Proc. Natl. Acad. Sci. U. S. A.* **2017**, *114* (16), E3205−E3214.

(16) Machovina, M. M.; Mallinson, S. J. B.; Knott, B. C.; Meyers, A. W.; Garcia-Borràs, M.; Bu, L.; Gado, J. E.; Oliver, A.; Schmidt, G. P.; Hinchen, D. J.; Crowley, M. F.; Johnson, C. W.; Neidle, E. L.; Payne, C. M.; Houk, K. N.; Beckham, G. T.; McGeehan, J. E.; DuBois, J. L. Enabling Microbial Syringol Conversion through Structure-Guided Protein Engineering. *Proc. Natl. Acad. Sci. U. S. A.* **2019**, *116* (28), 13970−13976.

(17) Groves, J. T. Key Elements of the Chemistry of Cytochrome P-450: The Oxygen Rebound Mechanism. *J. Chem. Educ.* **1985**, *62* (11), 928.

(18) Dawson, J. H.; Sono, M. Cytochrome P-450 and Chloroperoxidase: Thiolate-Ligated Heme Enzymes. Spectroscopic Determination of Their Active-Site Structures and Mechanistic Implications of Thiolate Ligation. *Chem. Rev.* **1987**, *87* (5), 1255−1276.

(19) Ortiz de Montellano, P. R.; De Voss, J. J. Oxidizing Species in the Mechanism of Cytochrome P450. *Nat. Prod. Rep.* **2002**, *19* (4), 477−493.

(20) De Montellano, P. R. O. In *Cytochrome P450*; de Montellano, P. R. O., Ed.; Springer US: Boston, MA, 2005.

(21) Poulos, T. L.; Johnson, E. F. Structures of Cytochrome P450 Enzymes. In *Cytochrome P450*; Springer US: Boston, MA, 2005; pp 87−114.

(22) Guengerich, F. P.; Munro, A. W. Unusual Cytochrome P450 Enzymes and Reactions. *J. Biol. Chem.* **2013**, *288* (24), 17065−17073.

(23) Munro, A. W.; McLean, K. J.; Grant, J. L.; Makris, T. M. Structure and Function of the Cytochrome P450 Peroxygenase Enzymes. *Biochem. Soc. Trans.* **2018**, *46* (1), 183−196.

(24) Huang, X.; Groves, J. T. Oxygen Activation and Radical Transformations in Heme Proteins and Metalloporphyrins. *Chem. Rev.* **2018**, *118* (5), 2491−2553.

(25) Kamachi, T.; Yoshizawa, K. A Theoretical Study on the Mechanism of Camphor Hydroxylation by Compound I of Cytochrome P450. *J. Am. Chem. Soc.* **2003**, *125* (15), 4652−4661.

(26) Ortiz de Montellano, P. R. Hydrocarbon Hydroxylation by Cytochrome P450 Enzymes. *Chem. Rev.* **2010**, *110* (2), 932−948.

(27) Ortiz de Montellano, P. R. Cytochrome P-450 Catalysis: Radical Intermediates and Dehydrogenation Reactions. *Trends Pharmacol. Sci.* **1989**, *10* (9), 354−359.

(28) Guengerich, F. P. Human Cytochrome P450 Enzymes. In *Cytochrome P450*; Springer US: Boston, MA, 1995; pp 473−535.

(29) de Montellano, P. R. O. Oxygen Activation and Reactivity. In *Cytochrome P450*; Springer US: Boston, MA, 1995; pp 245−303.

(30) Poulos, T. L.; Cupp-Vickery, J.; Li, H. Structural Studies on Prokaryotic Cytochromes P450. In *Cytochrome P450*; Springer US: Boston, MA, 1995; pp 125−150.

(31) Sono, M.; Roach, M. P.; Coulter, E. D.; Dawson, J. H. Heme-Containing Oxygenases. *Chem. Rev.* **1996**, *96* (7), 2841−2888.

(32) Guengerich, F. P. CYTOCHROME P-450 3A4: Regulation and Role in Drug Metabolism. *Annu. Rev. Pharmacol. Toxicol.* **1999**, *39* (1), 1−17.

(33) Sligar, S. G. Nature's Universal Oxygenases: The Cytochromes P450. *Essays Biochem.* **1999**, *34*, 71−83.

(34) Watanabe, Y. Alternatives to the Oxoferryl Porphyrin Cation Radical as the Proposed Reactive Intermediate of Cytochrome P450: Two-Electron Oxidized Fe(III) Porphyrin Derivatives. *JBIC, J. Biol. Inorg. Chem.* **2001**, *6* (8), 846−856.

(35) Shaik, S.; Hirao, H.; Kumar, D. Reactivity of High-Valent Iron−Oxo Species in Enzymes and Synthetic Reagents: A Tale of Many States. *Acc. Chem. Res.* **2007**, *40* (7), 532−542.
(36) Shaik, S.; Hirao, H.; Kumar, D. Reactivity Patterns of Cytochrome P450 Enzymes: Multifunctionality of the Active Species, and the Two States−Two Oxidants Conundrum. *Nat. Prod. Rep.* **2007**, *24* (3), 533−552.
(37) Yamamoto, S.; Kashiwagi, H. CASSCF Study on the Fe-O2 Bond in a Dioxygen Heme Complex. *Chem. Phys. Lett.* **1989**, *161* (1), 85−89.
(38) Loew, G. H.; Harris, D. L. Role of the Heme Active Site and Protein Environment in Structure, Spectra, and Function of the Cytochrome P450s. *Chem. Rev.* **2000**, *100* (2), 407−420.
(39) Harris, D. L. High-Valent Intermediates of Heme Proteins and Model Compounds. *Curr. Opin. Chem. Biol.* **2001**, *5* (6), 724−735.
(40) Shaik, S.; de Visser, S. P.; Ogliaro, F.; Schwarz, H.; Schröder, D. Two-State Reactivity Mechanisms of Hydroxylation and Epoxidation by Cytochrome P-450 Revealed by Theory. *Curr. Opin. Chem. Biol.* **2002**, *6* (5), 556−567.
(41) Shaik, S.; De Visser, S. P. Computational Approaches to Cytochrome P450 Function. In *Cytochrome P450*; Springer US: Boston, MA, 2005; pp 45−85.
(42) Shaik, S.; Kumar, D.; de Visser, S. P.; Altun, A.; Thiel, W. Theoretical Perspective on the Structure and Mechanism of Cytochrome P450 Enzymes †. *Chem. Rev.* **2005**, *105* (6), 2279−2328.
(43) Ichinose, H. Cytochrome P450 of Wood-Rotting Basidiomycetes and Biotechnological Applications. *Biotechnol. Appl. Biochem.* **2013**, *60* (1), 71−81.
(44) García-Hidalgo, J.; Ravi, K.; Kuré, L.-L.; Lidén, G.; Gorwa-Grauslund, M. Identification of the Two-Component Guaiacol Demethylase System from Rhodococcus Rhodochrous and Expression in Pseudomonas Putida EM42 for Guaiacol Assimilation. *AMB Express* **2019**, *9* (1), 34.
(45) Park, H.; Park, G.; Jeon, W.; Ahn, J.-O.; Yang, Y.-H.; Choi, K.-Y. Whole-Cell Biocatalysis Using Cytochrome P450 Monooxygenases for Biotransformation of Sustainable Bioresources (Fatty Acids, Fatty Alkanes, and Aromatic Amino Acids). *Biotechnol. Adv.* **2020**, *40*, 107504.
(46) Tumen-Velasquez, M.; Johnson, C. W.; Ahmed, A.; Dominick, G.; Fulk, E. M.; Khanna, P.; Lee, S. A.; Schmidt, A. L.; Linger, J. G.; Eiteman, M. A.; et al. Accelerating Pathway Evolution by Increasing the Gene Dosage of Chromosomal Segments. *Proc. Natl. Acad. Sci. U. S. A.* **2018**, *115* (27), 7105−7110.
(47) Mallinson, S. J. B.; Machovina, M. M.; Silveira, R. L.; Garcia-Borràs, M.; Gallup, N.; Johnson, C. W.; Allen, M. D.; Skaf, M. S.; Crowley, M. F.; Neidle, E. L.; et al. A Promiscuous Cytochrome P450 Aromatic O-Demethylase for Lignin Bioconversion. *Nat. Commun.* **2018**, *9* (1), 2487.
(48) Ali, H. S.; Henchman, R.; de Visser, S. P. Lignin Biodegradation by a Cytochrome P450 Enzyme: A Computational Study into Syringol Activation by GcoA. *Chem. - Eur. J.* **2020**, *26*, 13093.
(49) Csermely, P. Creative Elements: Network-Based Predictions of Active Centres in Proteins and Cellular and Social Networks. *Trends Biochem. Sci.* **2008**, *33* (12), 569−576.
(50) Vishveshwara, S.; Ghosh, A.; Hansia, P. Intra and Inter-Molecular Communications Through Protein Structure Network. *Curr. Protein Pept. Sci.* **2009**, *10* (2), 146−160.
(51) DeYonker, N. J.; Webster, C. E. Phosphoryl Transfers of the Phospholipase D Superfamily: A Quantum Mechanical Theoretical Study. *J. Am. Chem. Soc.* **2013**, *135* (37), 13764−13774.
(52) DeYonker, N. J.; Webster, C. E. A Theoretical Study of Phosphoryl Transfers of Tyrosyl-DNA Phosphodiesterase I (Tdp1) and the Possibility of a "Dead-End" Phosphohistidine Intermediate. *Biochemistry* **2015**, *54* (27), 4236−4247.
(53) Cheng, Q.; DeYonker, N. J. Acylation and Deacylation Mechanism and Kinetics of Penicillin G Reaction with Streptomyces R61 DD -peptidase. *J. Comput. Chem.* **2020**, *41* (18), 1685−1697.
(54) Summers, T. J.; Cheng, Q.; DeYonker, N. J. A Transition State "Trapped"? QM-Cluster Models of Engineered Threonyl-TRNA Synthetase. *Org. Biomol. Chem.* **2018**, *16* (22), 4090−4100.
(55) Jindal, G.; Warshel, A. Exploring the Dependence of QM/MM Calculations of Enzyme Catalysis on the Size of the QM Region. *J. Phys. Chem. B* **2016**, *120* (37), 9913−9921.
(56) Mehmood, R.; Kulik, H. J. Both Configuration and QM Region Size Matter: Zinc Stability in QM/MM Models of DNA Methyltransferase. *J. Chem. Theory Comput.* **2020**, *16* (5), 3121−3134.
(57) Word, J. M.; Lovell, S. C.; Richardson, J. S.; Richardson, D. C. Asparagine and Glutamine: Using Hydrogen Atom Contacts in the Choice of Side-Chain Amide Orientation 1 1Edited by J. Thornton. *J. Mol. Biol.* **1999**, *285* (4), 1735−1747.
(58) Word, J. M.; Lovell, S. C.; LaBean, T. H.; Taylor, H. C.; Zalis, M. E.; Presley, B. K.; Richardson, J. S.; Richardson, D. C. Visualizing and Quantifying Molecular Goodness-of-Fit: Small-Probe Contact Dots with Explicit Hydrogen Atoms 1 1Edited by J. Thornton. *J. Mol. Biol.* **1999**, *285* (4), 1711−1733.
(59) Frisch, M. J.; Trucks, G. W.; Schlegel, H. B.; Scuseria, G. E.; Robb, M. A.; Cheeseman, J. R.; Scalmani, G.; Barone, V.; Petersson, G. A.; Nakatsuji, H.; et al. *Gaussian 16*, Rev. B.01; 2016.
(60) Lee, C.; Yang, W.; Parr, R. G. Development of the Colle-Salvetti Correlation-Energy Formula into a Functional of the Electron Density. *Phys. Rev. B: Condens. Matter Mater. Phys.* **1988**, *37* (2), 785−789.
(61) Becke, A. D. Density-Functional Thermochemistry. {III. The} Role of Exact Exchange. *J. Chem. Phys.* **1993**, *98*, 5648−5652.
(62) Hariharan, P. C.; Pople, J. A. The Influence of Polarization Functions on Molecular Orbital Hydrogenation Energies. *Theor. Chim. Acta* **1973**, *28* (3), 213−222.
(63) Petersson, G. A.; Al-Laham, M. A. A Complete Basis Set Model Chemistry. II. Open-Shell Systems and the Total Energies of the First-Row Atoms. *J. Chem. Phys.* **1991**, *94* (9), 6081−6090.
(64) Foresman, J. B.; Frisch, Æ. *Exploring Chemistry with Electronic Structure Methods*, 2nd ed.; Gaussian Inc., Pittsburgh, PA 1996; pp 266, 278−283.
(65) Dunning, T. H.; Hay, P. J. Gaussian Basis Sets for Molecular Calculations. In *Methods of Electronic Structure Theory*; Springer US: Boston, MA, 1977; pp 1−27.
(66) Hay, P. J.; Wadt, W. R. Ab Initio Effective Core Potentials for Molecular Calculations. Potentials for K to Au Including the Outermost Core Orbitals. *J. Chem. Phys.* **1985**, *82* (1), 299−310.
(67) Wadt, W. R.; Hay, P. J. Ab Initio Effective Core Potentials for Molecular Calculations. Potentials for Main Group Elements Na to Bi. *J. Chem. Phys.* **1985**, *82* (1), 284−298.
(68) Hehre, W. J.; Ditchfield, R.; Pople, J. A. Self—Consistent Molecular Orbital Methods. XII. Further Extensions of Gaussian—Type Basis Sets for Use in Molecular Orbital Studies of Organic Molecules. *J. Chem. Phys.* **1972**, *56* (5), 2257−2261.
(69) Grimme, S.; Ehrlich, S.; Goerigk, L. Effect of the Damping Function in Dispersion Corrected Density Functional Theory. *J. Comput. Chem.* **2011**, *32* (7), 1456−1465.
(70) Grimme, S.; Antony, J.; Ehrlich, S.; Krieg, H. A Consistent and Accurate Ab Initio Parametrization of Density Functional Dispersion Correction (DFT-D) for the 94 Elements H-Pu. *J. Chem. Phys.* **2010**, *132* (15), 154104.
(71) Barone, V.; Cossi, M. Quantum Calculation of Molecular Energies and Energy Gradients in Solution by a Conductor Solvent Model. *J. Phys. Chem. A* **1998**, *102* (11), 1995−2001.
(72) Cossi, M.; Rega, N.; Scalmani, G.; Barone, V. Energies, Structures, and Electronic Properties of Molecules in Solution with the C-PCM Solvation Model. *J. Comput. Chem.* **2003**, *24* (6), 669−681.
(73) Siegbahn, P. E. M.; Blomberg, M. R. A. Transition-Metal Systems in Biochemistry Studied by High-Accuracy Quantum Chemical Methods. *Chem. Rev.* **2000**, *100* (2), 421−438.
(74) Blomberg, M. R. A.; Borowski, T.; Himo, F.; Liao, R.-Z.; Siegbahn, P. E. M. Quantum Chemical Studies of Mechanisms for Metalloenzymes. *Chem. Rev.* **2014**, *114* (7), 3601−3658.
(75) Fukui, K. Formulation of the Reaction Coordinate. *J. Phys. Chem.* **1970**, *74* (23), 4161−4163.
(76) Fukui, K. The Path of Chemical Reactions - the IRC Approach. *Acc. Chem. Res.* **1981**, *14* (12), 363−368.

https://doi.org/10.1021/acs.jpcb.0c10761
J. Phys. Chem. B 2021, 125, 3296−3306

(77) Fujii, Y.; Hata, M.; Hoshino, T.; Tsuda, M. Catalytic Mechanism of Class A β-Lactamase: Role of Lysine 73 and C3-Carboxyl Group of the Substrate Pen G in the Deacylation Step. *J. Phys. Chem. B* **2002**, *106* (37), 9687−9695.
(78) Stone, K. L.; Behan, R. K.; Green, M. T. X-Ray Absorption Spectroscopy of Chloroperoxidase Compound I: Insight into the Reactive Intermediate of P450 Chemistry. *Proc. Natl. Acad. Sci. U. S. A.* **2005**, *102* (46), 16563−16565.
(79) Cohen, S.; Kumar, D.; Shaik, S. In Silico Design of a Mutant of Cytochrome P450 Containing Selenocysteine. *J. Am. Chem. Soc.* **2006**, *128* (8), 2649−2653.
(80) Meunier, B.; de Visser, S. P.; Shaik, S. Mechanism of Oxidation Reactions Catalyzed by Cytochrome P450 Enzymes. *Chem. Rev.* **2004**, *104* (9), 3947−3980.
(81) Schöneboom, J. C.; Cohen, S.; Lin, H.; Shaik, S.; Thiel, W. Quantum Mechanical/Molecular Mechanical Investigation of the Mechanism of C−H Hydroxylation of Camphor by Cytochrome P450 c Am : Theory Supports a Two-State Rebound Mechanism. *J. Am. Chem. Soc.* **2004**, *126* (12), 4017−4034.
(82) Shaik, S.; Cohen, S.; Wang, Y.; Chen, H.; Kumar, D.; Thiel, W. P450 Enzymes: Their Structure, Reactivity, and Selectivity—Modeled by QM/MM Calculations. *Chem. Rev.* **2010**, *110* (2), 949−1017.
(83) Guallar, V.; Baik, M.-H.; Lippard, S. J.; Friesner, R. A. Peripheral Heme Substituents Control the Hydrogen-Atom Abstraction Chemistry in Cytochromes P450. *Proc. Natl. Acad. Sci. U. S. A.* **2003**, *100* (12), 6998−7002.

https://doi.org/10.1021/acs.jpcb.0c10761
J. Phys. Chem. B 2021, 125, 3296−3306